

A Novel Approach to Industrial Defect Generation through Blended Latent Diffusion Model with Online Adaptation

Hanxi Li^{1,2,†}, Zhengxun Zhang^{1,2,†}, Hao Chen^{2,*}, Lin Wu *Senior Member, IEEE*^{3,*}, Bo Li⁴, Deyin Liu⁵, and Mingwen Wang¹

¹Jiangxi Normal University, Jiangxi, China

²Zhejiang University, Zhejiang, China

³Department of Computer Science, Swansea University, SA1 8EN, United Kingdom

⁴Northwestern Polytechnical University, Shannxi, China

⁵Zhengzhou University, Henan, China

[†]These authors contributed equally to this work

^{*}Corresponding author

Abstract—Effectively addressing the challenge of industrial Anomaly Detection (AD) necessitates an ample supply of defective samples, a constraint often hindered by their scarcity in industrial contexts. This paper introduces a novel algorithm designed to augment defective samples, thereby enhancing AD performance. The proposed method tailors the blended latent diffusion model for defect sample generation, employing a diffusion model to generate defective samples in the latent space. A feature editing process, controlled by a “trimap” mask and text prompts, refines the generated samples. The image generation inference process is structured into three stages: a free diffusion stage, an editing diffusion stage, and an online decoder adaptation stage. This sophisticated inference strategy yields high-quality synthetic defective samples with diverse pattern variations, leading to significantly improved AD accuracies based on the augmented training set. Specifically, on the widely recognized MVTec AD dataset, the proposed method elevates the state-of-the-art (SOTA) performance of AD with augmented data by 1.5%, 1.9%, and 3.1% for AD metrics AP, IAP, and IAP90, respectively. The implementation code of this work can be found at the GitHub repository <https://github.com/GrandpaXun242/AdaBLDM.git>

Index Terms—Anomaly detection, Blended latent diffusion model, Online adaption.

I. INTRODUCTION

In a practical manufacturing workflow, obtaining defective samples is considerably more challenging compared to acquiring defect-free ones. Consequently, the majority of recently proposed algorithms for industrial defect inspection, such as [1]–[10], address the issue as an Anomaly Detection (AD) problem—an established machine learning challenge [11], [12]. Among these industrial AD algorithms, the assumption is made that all anomaly-free samples, be they complete images or image patches, belong to a single distribution. Meanwhile, defective samples are identified as “outliers”. The strategic choice of adopting an Anomaly Detection approach for industrial defect inspection is evident: the absence of the

This work was conducted during Hanxi Li’s visit to Zhejiang University.

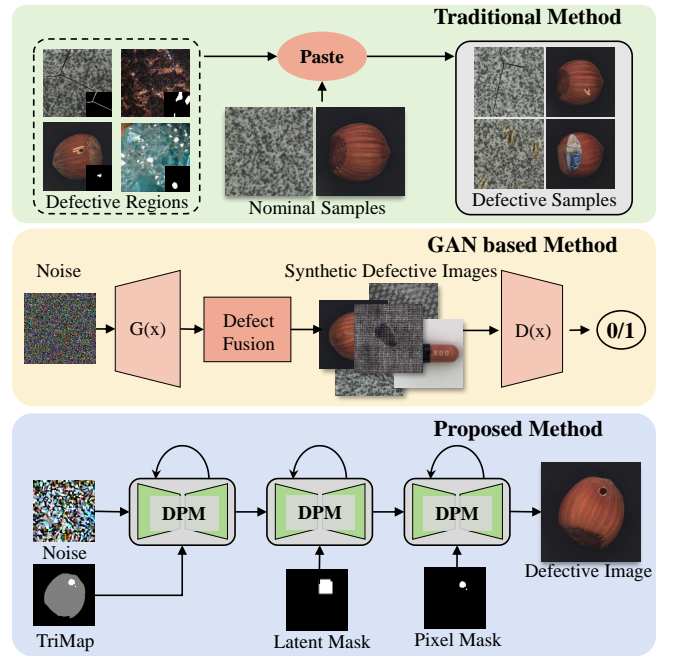


Fig. 1. Illustration of three defect generation styles. From top to bottom: conventional approaches, GAN-based algorithms, and the proposed method.

need for defective samples during the training stage makes these AD-based algorithms inherently compatible with practical manufacturing scenarios.

Nonetheless, achieving this compatibility comes at the expense of an extremely imbalanced data distribution, a characteristic that is deemed unacceptable in the context of most discriminative algorithms. Consequently, some researchers suggest the generation of artificial defect patterns using conventional approaches [1], [3], [5] to facilitate subsequent discriminative learning processes. Recently, state-of-the-art (SOTA) algorithms [13]–[15] suggest that incorporating a few real

anomalous samples during the training stage can significantly enhance the AD accuracy if these samples are combined with synthetic samples. For example, some pioneering works [16], [17] demonstrated the benefits of generating these “lifelike” defects using more sophisticated methods. The first two rows of Fig. I illustrate two different types of defect generation.

In this paper, we propose the integration of the cutting-edge AI generation algorithm, namely the Diffusion Probabilistic Model (DPM) [18], into the realm of defect generation. Specifically, we leverage the Blended Latent Diffusion Model [19]–[21] to create our framework. To enhance the generation of defective samples, we innovate the Blended Latent Diffusion Model (BLDM) [21] with three modules. First, we design a novel “defect trimap” to delineate the target object mask and the defective regions on the generated image, incorporating it as a new form of controlling information alongside the language prompts within the stable diffusion model. Second, to ensure the authenticity of the generated samples, a cascaded “editing” stage is introduced into the BLDM, at both the latent and pixel space. Finally, an innovative online adaptation of the image encoder is proposed to refine the quality of the generated images. Consequently, the customized BLDM algorithm, referred to as AdaBLDM in this paper, is capable of generating higher-quality defective samples with pattern variations. The third row of Fig. I provides a brief illustration of the proposed BLDM-based method. In summary, the contributions of this paper are threefold, as outlined below.

- To the best of our knowledge, it is the first time that the Diffusion Model has been adopted for the task of industrial defect generation. The advantages of the BLDM such as the generation stability, the high image quality, and the controllable content could all contribute to achieving a better defect generator compared with the SOTA methods.
- To tailor the BLDM algorithm to the defect generation scenario, we bake BLDM in the aspects of controlling information, preheating stage, and online adaptation, respectively. This endeavor leads to the proposed algorithm, termed AdaBLDM, which achieves notably improved defective samples compared to synthetic ones generated by existing SOTA methods.
- Given the defective samples generated by the proposed method, we achieved new SOTA performance on the MVTec AD dataset [22]. In specific, the proposed AdaBLDM outperforms the best-to-date method DeSTseg [6] by **1.5%**, **1.9%**, **3.1%** on the AD metrics AP, IAP and IAP90, respectively.

The remainder of this paper is organized as follows. In Sec. II, we discussed the related work in literature. The section III presents the proposed method in detail. Experimental results and the ablation study are addressed in Sec. IV. We conclude this paper in Sec. V.

II. RELATED WORK

A. Synthetic Defect Generation

Due to the scarcity of defective samples, generating synthetic defective samples becomes a rule of thumb among researchers to achieve satisfactory performance [1]–[3], [5],

[6], [23]. A straightforward way akin to data augmentation is mimicking the defects by “pasting” anomalous pixels on the normal images. For example, methods in the regime [1], [24], [25] randomly cut regions from normal images and paste them to the “incorrect” places as artificial defects. Crop&Paste [26] and PRN [27] crop defect areas from genuine defective images and paste them onto defect-free images. Those algorithms, though achieve better AD performance compared with the standard one-class AD approaches, can not create new defect patterns and thus likely lead to overfitting problems. To increase the variations of anomalies, DRAEM [3], DeSTseg [6], MegSeg [5] and ReSynthDetect [28] employ extra datasets combined with Berlin noise to fabricate defects. However, in these cases, the distribution of fabricated defects differs from the real one and thus the performance gain can not be ensured.

Inspired by the potent AIGC (AI Generated Contents) methods such as Generative Adversarial Network (GAN) based algorithms [29]–[31] and diffusion model-based algorithms [32], some attempts have been devoted to generating more natural-looking simulated defects. In particular, SDGAN [30] employs two generators to switch the defective and non-defective status for sample images. As a result, SDGAN [30] can generate a high-quality, diverse dataset of steel surfaces with both defective and defect-free images. In a similar vein to SDGAN [30], Defect-GAN [33] converts non-defective images into defective ones to enhance the learning process of the defect classifier. However, the above two GAN-based generation algorithms cannot generate defective regions that are aligned precisely as required. Despite that they could enhance the performance of defect classification, they cannot lift the defect segmentation accuracy which is crucial in many real-world applications.

More recently, [16] and [17] proposed to generate both synthetic defective images and the corresponding pixel-level labels. In specific, the DCDGANc algorithm [16] designed a novel GAN-based method to mimic real defects, which can be fused with defect-free images via an improved Poisson blending algorithm. At the same time, [17] introduced DFM-GAN, stemming from StyleGANv2 [34], to generate defective images and defective masks by using the proposed defect-aware residual blocks. Although the above two GAN-based methods can generate high-quality images with defects, they fall short in generating the defective mass strictly aligned to the generated defective pixels on the image. Such misalignment is ascribed to the disparity between the image-specific generative methods and the challenging scenario of AD, and thus significantly misleads the defective segmentation model in AD. In contrast, in this paper, we propose a novel defect generation method based on Diffusion Models. We tame this general-purpose algorithm to generate diverse, realistic but accurately-controlled defective image samples via a series of novel modifications.

B. Diffusion Probabilistic Models for Image Editing

In the last few years, researchers have proposed various approaches to realize high-quality image generation. The off-the-shelf tools include Generative Adversarial Networks (GANs)

[35], Variational AutoEncoders (VAEs) [36], the flow-based algorithms [37], and Diffusion Probabilistic Models (DPMs) [18], [38]–[40]. In specific, DPMs have demonstrated higher qualities of the synthetic images and impressive stability of training. Accordingly, the DPM-based approaches, such as Stable Diffusion (Stability AI) [19], DALL-E2 (OpenAI) [41], and Imagen (Google) [42], have achieved state-of-the-art performances in the task of content generation.

DPM-based methods also play an important role in the remit of image editing. In particular, the Latent Diffusion Model [19] conducts the image generation or editing in the lower-dimensional latent space and thus can achieve higher efficiency; RePaint [43] fully leverages a pre-trained DDPM [39] to perform image editing by sampling given pixels during the reverse diffusion stage; DCFace [44] employs two feature encoders to control the Diffusion Model to facilitate facial image editing; [45] proposes the “ControlNet” to govern existing Diffusion models to achieve a better-controlled synthesis; [20], [21] enable image editing by making modifications in either the pixel space or feature space; [46] propose the “Dual-Cycle Diffusion” to generate an unbiased mask to guide image editing. While these methods demonstrate state-of-the-art (SOTA) performances in general image editing tasks, they can hardly produce image regions that are precisely aligned at the pixel level due to the inherently fuzzy nature of the reverse diffusion process. This nuisance can potentially decrease the segmentation capacity in anomaly detection.

In this paper, we customize the cutting-edge Blended Latent Diffusion Model (BLDM) [21] to generate precisely aligned synthetic regions for industrial defect detection and localization. It is important to note that this work employs the diffusion model for generating synthetic images or image regions, just similar to the pioneering work [18], [47] proposed for the general editing tasks. Our method is irrelevant to the algorithms that use DPM to directly predict anomaly regions on the test images [48]–[51].

III. THE PROPOSED METHOD

A. Task Definition and Preliminaries

Following the conventional setting of anomaly detection, an anomaly-free (OK) sample set $\mathcal{X}_{OK} = \{\mathbf{x}_{OK}^i \in \mathbb{R}^{H_x \times W_x \times 3} \mid i = 1, 2, \dots, N_{OK}\}$ is available for training. Furthermore, as introduced in Sec. I, a few defective (NG) samples $\mathcal{X}_{NG} = \{\mathbf{x}_{NG}^i \in \mathbb{R}^{H_x \times W_x \times 3} \mid i = 1, 2, \dots, N_{NG}\}$ and the corresponding anomaly masks $\mathcal{M}_{NG} = \{\mathbf{M}_{NG}^i \in \mathbb{B}^{H_x \times W_x} \mid i = 1, 2, \dots, N_{NG}\}$ are given as the “seeds” of defect generation and usually $N_{NG} \ll N_{OK}$. The goal of the proposed method is to generate a number of training samples with synthetic defective regions, *i.e.*,

$$\{\mathcal{X}_{OK}, \mathcal{X}_{NG}, \mathcal{M}_{NG}\} \xrightarrow{\text{Defect Generator}} \{\mathcal{X}_{NG}^*, \mathcal{M}_{NG}^*\}, \quad (1)$$

where $\mathcal{X}_{NG}^* = \{\mathbf{x}_{NG}^{*i} \in \mathbb{R}^{H_x \times W_x \times 3} \mid i = 1, 2, \dots, N_{NG}^*\}$ and $\mathcal{M}_{NG}^* = \{\mathbf{M}_{NG}^{*i} \in \mathbb{B}^{H_x \times W_x} \mid i = 1, 2, \dots, N_{NG}^*\}$ comprise the obtained synthetic samples and the corresponding defect masks, respectively. Furthermore, usually we set $N_{NG}^* \gg N_{NG}$ to ensure high pattern variation of the generated samples.

In this paper, we propose to generate the synthetic samples using a diffusion model. It is common for diffusion models [18], [38] to approach generation target as a noise-free variable \mathbf{x}_0 and define the “forward diffusion process” as follows

$$\begin{aligned} q(\mathbf{x}_t \mid \mathbf{x}_{t-1}) &= \mathcal{N}(\mathbf{x}_t; \sqrt{1 - \beta_t} \mathbf{x}_{t-1}, \beta_t \mathbf{I}) \\ q(\mathbf{x}_{1:T} \mid \mathbf{x}_0) &= \prod_{t=1}^T q(\mathbf{x}_t \mid \mathbf{x}_{t-1}), \end{aligned} \quad (2)$$

where $\{\beta_t \in (0, 1)\}_{t=1}^T$ denotes the predefined variance schedule and \mathbf{I} is a identity matrix. When T is large enough, the diffusion process could convert a normal image into a random noise \mathbf{x}_T . On the contrary, the “reverse diffusion process” is defined as

$$\begin{aligned} p_\theta(\mathbf{x}_{t-1} \mid \mathbf{x}_t) &= \mathcal{N}(\mathbf{x}_{t-1}; \boldsymbol{\mu}_\theta(\mathbf{x}_t, t), \boldsymbol{\Sigma}_\theta(\mathbf{x}_t, t)) \\ p_\theta(\mathbf{x}_{0:T}) &= p(\mathbf{x}_T) \prod_{t=1}^T p_\theta(\mathbf{x}_{t-1} \mid \mathbf{x}_t), \end{aligned} \quad (3)$$

where $\boldsymbol{\mu}_\theta(\cdot)$ and $\boldsymbol{\Sigma}_\theta(\cdot)$ are the two unknown functions that are usually approximated as deep models. In the test phase, given different random Gaussian noise samples $\mathbf{x}_T^i, i = 1, \dots, N_{test}$, one could obtain high quality and various samples $\mathbf{x}_0^i, \forall i$ (usually RGB images) from the same domain of the training samples. Akin to the above diffusion process, we could also generate lifelike anomalous images in \mathcal{X}_{NG}^* based on a diffusion model which has been well learned on the samples sets \mathcal{X}_{OK} and \mathcal{X}_{NG} .

B. Latent Diffusion Model and Cross-Modal Prompts

1) *Latent diffusion model with controlling information:* In this paper, we employ the Latent Diffusion Model (LDM) as the backbone of our method encouraged by its praiseworthy advantages [19]. As the name indicating, the forward and reverse diffusion processes of LDM are both performed in the lower-dimensional latent space. Given an input image $\mathbf{x} \in \mathbb{R}^{H_x \times W_x \times 3}$, its corresponding latent feature $\mathbf{z} \in \mathbb{R}^{H_z \times W_z \times C_z}$ is obtained using the encoder function $\Omega(\cdot)$ as $\mathbf{z} = \Omega(\mathbf{x})$ while the image can also be recovered from \mathbf{z} via the decoding operation as $\mathbf{x} = \Phi(\mathbf{z})$. Based on the latent feature \mathbf{z} and some simplifications¹ from Eq. 3, the reverse conditional probability in latent space is revised as

$$\begin{aligned} p_\theta(\mathbf{z}_{t-1} \mid \mathbf{z}_t, t, \mathcal{C}) &= \\ \mathcal{N}\left(\mathbf{z}_{t-1}; \frac{1}{\sqrt{\alpha_t}} \left(\mathbf{z}_t - \frac{1 - \alpha_t}{\sqrt{1 - \bar{\alpha}_t}}\right) \epsilon_\theta(\mathbf{z}_t, t, \mathcal{C}), \sigma_t \mathbf{I}\right), \end{aligned} \quad (4)$$

where $\epsilon_\theta(\cdot)$ stands for the θ -parameterized deep model to be trained; \mathcal{C} denotes the controlling prompts fed into LDM for stabilizing the generation process [19]; α_t , $\bar{\alpha}_t$ and σ_t the parameters which can be calculated in a deterministic way at each t -th step. In our method, we propose to generate cross-modal controlling features to enhance the quality of the synthetic defect.

¹Readers are referred to [19] and [38] for more details

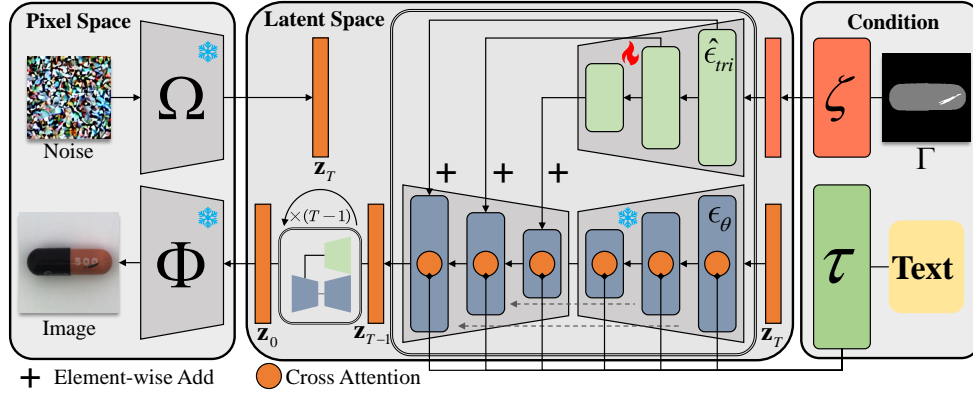


Fig. 2. The network structure of the proposed BLDM-based method for generating defective regions on a image. One can see besides the noise input, the model is governed by a text prompt and a trimap that indicates the locations of the object and defect

2) *Linguistic prompts*: As an effective module, linguistic prompts are introduced to control and stabilize the generation process of diffusion models [19], [21]. In this work, the linguistic prompt y is obtained by specifying the keywords in the following template sentence

$$y := \{\text{"obj"}\}, \text{a } \{\text{obj}\} \text{ with a } \{\text{def}\}, \quad (5)$$

where the keywords *obj* and *def* denote the category of the current object (as the capsule in Fig. 2) and defect type (as the black contamination on the capsule), respectively. One can see this template design is straightforward and thus the prompt is always easy to obtain. The sentence y is then processed by the parameter-frozen text encoder $\tau(\cdot) : \mathbb{R}^{d_y} \rightarrow \mathbb{R}^{d_{lang}}$ of the CLIP model [52]. In particular, as shown in Fig. 2, the linguistic controlling information is fed into the generation model $\epsilon_\theta(\cdot)$ and the generation process is governed via a K-Q-V attention mechanism proposed in [19].

3) *Defect trimap prompts*: Recall that in practical anomaly detection tasks, the defect-free samples are usually sufficient in terms of both amount and pattern variation, we thus propose to generate defective samples based on defect-free prototypes, rather than generating them from scratch. In a nutshell, a “trimap” $\Gamma \in \mathbb{R}^{H_x \times W_x}$ is designed to specify the desired location of the generated object and the defect, as shown in Fig. 2. To obtain a proper trimap, we firstly estimate the foreground region² on a randomly selected defect-free image \mathbf{x}_{OK} by using the method proposed in [14] and save the foreground mask as $\mathbf{F} \in \mathbb{B}^{H_x \times W_x}$ with $\mathbf{F}(x, y) = 1$ indicating a foreground pixel at the coordinate $[x, y]$. Secondly, a synthetic defect mask is created based on a genuine anomaly mask randomly selected from set \mathcal{M}_{NG} . Formally, the generation of the novel anomaly mask writes:

$$\mathcal{M}_{NG} \xrightarrow{\text{rand. } i} \mathbf{M}_{NG}^i \xrightarrow{\text{rand. affine}} \mathbf{M}_{NG}^A \xrightarrow{\text{fit } \mathbf{F}} \mathbf{M}_{NG}^*, \quad (6)$$

where $\mathbf{M}_{NG}^i, \mathbf{M}_{NG}^A, \mathbf{M}_{NG}^* \in \mathbb{B}^{H_x \times W_x}$; “rand. i ” refers to a random index selection; “rand. affine” denotes a random affine transform while “fit \mathbf{F} ” stands for adjusting the location and scale of \mathbf{M}_{NG}^A so that the adjusted mask is entirely inside

the foreground region defined by \mathbf{F} . Finally, the value of each pixel on Γ are defined as follows

$$\Gamma(x, y) = \begin{cases} 1 & \text{if } \mathbf{M}_{NG}^*(x, y) = 1, \\ 0.5 & \text{else if } \mathbf{F}(x, y) = 1, \\ 0 & \text{else.} \end{cases} \quad (7)$$

As shown in Fig. 2, in the proposed AdaBLDM algorithm, the controlling trimap Γ is firstly embedded by a convolutional block as $\zeta(\Gamma) \in \mathbb{R}^{H_z \times W_z \times C_z}$. The embedding feature is then fed into an encoder network $\hat{\epsilon}_{tri}(\cdot)$ that shares the same structure and initial parameters with the denoising encoder of $\epsilon_\theta(\cdot)$, except that the original “spatial attention” module is replaced with a self-attention process over the embedded trimap features. The deep features extracted from different layers of $\hat{\epsilon}_{tri}(\cdot)$ are then injected into the corresponding layers of the denoising decoder of $\epsilon_\theta(\cdot)$ via element-wise addition (see Fig. 2).

C. Loss Function and Training Scheme

Given the cross-modal controlling features $\{\tau(y), \zeta(\Gamma)\}$, the learning objective of the proposed model is defined as:

$$L_{LDM} := \mathbb{E}_{\mathbf{z}_t, \mathbf{c}, \epsilon \sim \mathcal{N}(0, 1), t} [\|\epsilon - \epsilon_\theta(\mathbf{z}_t, t, \tau(y), \hat{\epsilon}_{tri}(\zeta(\Gamma)))\|_2^2], \quad (8)$$

where $\epsilon_\theta(\cdot)$ denotes the denoising model and $\hat{\epsilon}_{tri}$ stands for the encoder for the latent trimap features. In this work, the involved modules are learned with different training schemes as described below.

- $\epsilon_\theta(\cdot)$ is pre-trained by using the domain dataset (e.g., all training images of all the subcategories of MVTEC AD [22] for the experiments on this dataset). We keep $\epsilon_\theta(\cdot)$ frozen during model learning for each subcategory.
- The trimap feature encoder $\hat{\epsilon}_{tri}(\cdot)$ is initialized by the corresponding parameters of the original LDM model [19] and then fine-tuned for each subcategory based on the real defective samples
- The convolutional block $\zeta(\cdot)$ for trimap embedding is only learned based on the genuine anomaly samples from scratch.
- For the image encoder $\Omega(\cdot)$ and decoder $\Phi(\cdot)$, we follow [19] to deploy the corresponding modules of the VQ-VAE algorithm [53], which are fixed during the training.

²The area corresponding to the interested object

Algorithm 1: Multi-Stage Denoising with Editing

Input: Defect-Free Image \mathbf{x}_{OK} , Trimap Γ , Defect Mask \mathbf{M}_{NG}^* , Language Prompt y , Decoder $\Psi(\cdot)$, Encoder $\Omega(\cdot)$, Range Numbers T_1, T_2 and T_3 , Predefined Normal Distribution $\mathcal{N}(\mu_z, \sigma_z^2)$

Output: Blended Latent Feature \mathbf{z}_{NG}^*

```

1  $\mathbf{z}_{OK} \in \mathbb{R}^{H_z \times W_z \times C_z} \leftarrow \Omega(\mathbf{x}_{OK})$ 
2  $\mathbf{M}_{NG}^z \in \mathbb{B}^{H_z \times W_z} \leftarrow \text{Dilate\&DownSample}(\mathbf{M}_{NG}^*)$ 
3  $\mathbf{z}_t \leftarrow \text{RandSample}(\mathcal{N}(\mu_z, \sigma_z^2))$ 
4  $t = T_1 + T_2 + T_3$ 
5 Free Diffusion Stage */
6 while  $t > T_2 + T_3$  do
7    $\mathbf{z}_{t-1} \leftarrow \text{Denoise}(\mathbf{z}_t, \Gamma, y)$ 
8    $t = t - 1$ 
9 end
10 Latent Editing Stage */
11 while  $t > T_3$  do
12    $\mathbf{z}_t = \mathbf{z}_t \odot \mathbf{M}_{NG}^z + \mathbf{z}_{OK} \odot \neg \mathbf{M}_{NG}^z$ 
13    $\mathbf{z}_{t-1} \leftarrow \text{Denoise}(\mathbf{z}_t, \Gamma, y)$ 
14    $t = t - 1$ 
15 end
16 Image Editing Stage */
17 while  $t \geq 0$  do
18    $\mathbf{x}_t = \Psi(\mathbf{z}_t)$ 
19    $\mathbf{z}_t \leftarrow \Omega(\mathbf{x}_t \odot \mathbf{M}_{NG} + \mathbf{x}_{OK} \odot \neg \mathbf{M}_{NG})$ 
20    $\mathbf{z}_{t-1} \leftarrow \text{Denoise}(\mathbf{z}_t, \Gamma, y)$ 
21    $t = t - 1$ 
22 end
23 return  $\mathbf{z}_{NG}^* = \mathbf{z}_0$ 
```

- The text encoder $\tau(\cdot)$ is copied from CLIP and frozen during training.

D. Multi-Stage Denoising with Content Editing

In this paper, we propose to perform feature editing in the inference phase by tailoring the editing scheme of Blended Latent Diffusion (BLD) [20] for defect generation.

First of all, given a defect-free image \mathbf{x}_{OK} and a trimap Γ , the corresponding defect mask \mathbf{M}_{NG}^* is calculated as introduced in Sec. III-B3. Then the multi-stage denoising algorithm with content editing is performed and the workflow of this algorithm is illustrated in Alg. 1 where \odot indicates element-wise multiplication and \neg stands for the element-wise operation of logical “NOT” on the binary map.

As shown in Fig. 3, the pipeline consists of three stages in the denoising phase. The first stage takes T_1 steps to conduct the conventional denoising [19], [38], [39] without content editing. The second stage spends T_2 steps and the input feature \mathbf{z}_t is merged with the feature of \mathbf{x}_{OK} , under the guidance of the dilated defect mask \mathbf{M}_{NG}^* . In the third stage, a novel content blending method proposed in this paper is conducted. In specific, the blending operation is performed in the pixel space and the blended image is then remapped back to the latent space for denoising. The image encoder $\Omega(\cdot)$ and decoder $\Phi(\cdot)$ are used cooperatively to switch the information between the two spaces.

Algorithm 2: Online Decoder Adaptation

Input: Blended Latent Feature \mathbf{z}_{NG}^* , Defect-Free Image \mathbf{x}_{OK} , Maximum Step T_{ft} , Conservative Ratio λ_{con} , Anomaly Mask \mathbf{M}_{NG}^* , Decoder $\Phi(\cdot)$

Output: Refined Image \mathbf{x}_{NG}^*

```

1  $\mathbf{x}_{NG}^* \leftarrow \Phi(\mathbf{z}_{NG}^*)$ ,  $\bar{\mathbf{M}}_{NG}^*(i, j) \leftarrow \neg \mathbf{M}_{NG}^*(i, j)$ 
2  $t = 1$ 
3 while  $t \leq T_{ft}$  do
4    $\tilde{\mathbf{x}} \leftarrow \Phi(\mathbf{z}_{NG}^*)$ 
5    $L_i = \sum_{i,j}^{H_x W_x} (\tilde{\mathbf{x}}(i, j) - \mathbf{x}_{OK}(i, j))^2 \odot \bar{\mathbf{M}}_{NG}^*(i, j)$ 
6    $L_d = \sum_{i,j}^{H_x W_x} (\tilde{\mathbf{x}}(i, j) - \mathbf{x}_{NG}^*(i, j))^2 \odot \mathbf{M}_{NG}^*(i, j)$ 
7    $\Phi(\cdot) \leftarrow \text{AdamW}(L_i + \lambda_{con} L_d, \Phi(\cdot))$ 
8    $t = t + 1$ 
9 end
10  $\mathbf{x}_{NG}^* \leftarrow \Phi(\mathbf{z}_{NG}^*)$ 
11 return  $\mathbf{x}_{NG}^*$ 
```

E. Online Decoder Adaptation

Considering that the image quality of the synthetic defective sample can be significantly influenced by the image decoder $\Phi(\cdot)$, we propose to fine-tune the decoder for each generated sample. Once the blended latent feature $\mathbf{z}_{NG}^* \in \mathbb{R}^{H_z \times W_z \times C_z}$ is obtained from Alg. 1, and given the defective mask $\mathbf{M}_{NG}^* \in \mathbb{B}^{H_x \times W_x}$ and the source image $\mathbf{x}_{OK} \in \mathbb{R}^{H_x \times W_x \times 3}$, we can fine-tune the decoder model $\Phi(\cdot)$ by conducting the online update algorithm as described in Alg. 2, which shows that the online adaptation strategy encourages the decoder $\Phi(\cdot)$ generating defect-free pixels assembling to \mathbf{x}_{OK} and simultaneously outputting the defective pixels guided by the original decoder. The conservative ratio λ_{con} balances the two objectives. In the experiments of this paper, we demonstrate that this online-updated decoder can generate more realistic samples for AD training and thus leads to higher AD performance.

F. Implementation Details

In this paper, all the images are resized to 256×256 following the setting of DeSTseg [6] which is a SOTA anomaly detection algorithm adopted by this paper for evaluating the effectiveness of the generated samples. In this way, we set $H_x = W_x = 256$ and $H_z = W_z = 32$. The latent feature channel number C_z is 4 in this paper for efficient denoising operation. As to the trimap prompts, the object’s region is estimated by using the foreground estimation method proposed in [14] and the anomalous mask is obtained based on the randomly selected 10 genuine defective samples for each subcategory of the dataset. The affine transformation matrix mentioned in Sec. III-B3 is determined by a random rotation angle $\gamma \in [0^\circ, 360^\circ]$ and a random scaling factor $s \in [0.85, 1.15]$. For the AD tasks on texture subcategories, such as a wooden or a fabric surface, all the pixels are considered as foreground except the defective ones.

We employed the AdamW optimizer [54] for updating the model parameters, with a default learning rate of 1×10^{-5} , and default betas are set to 0.9 and 0.999, respectively. During

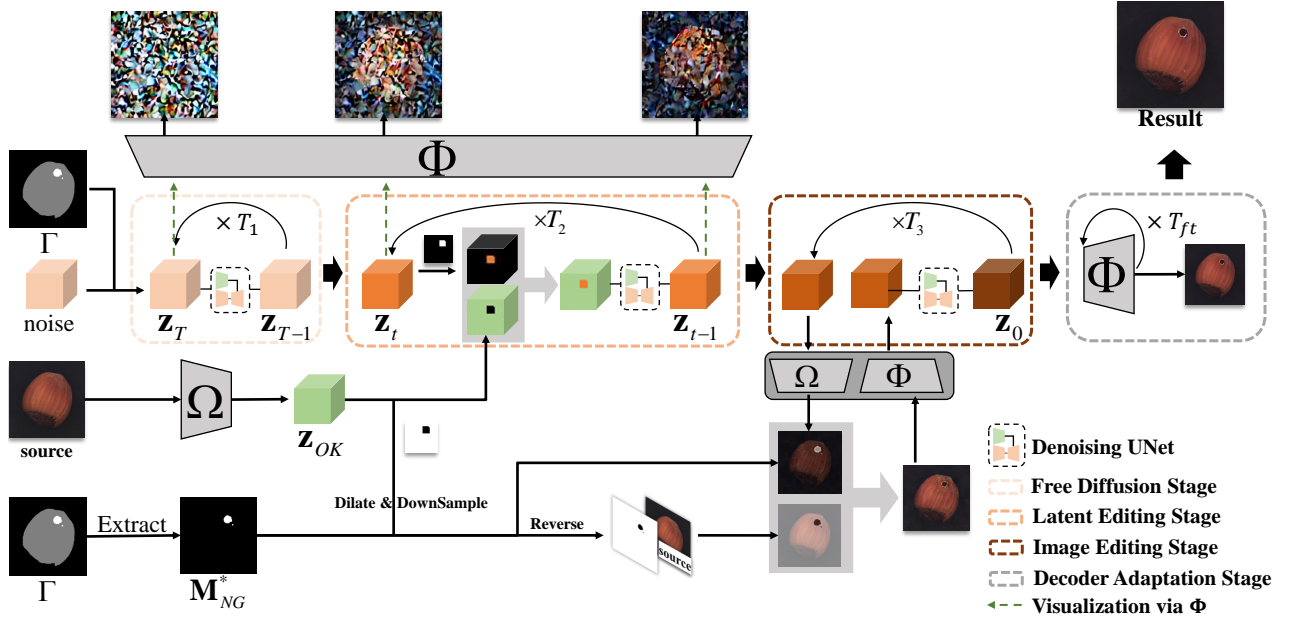


Fig. 3. The inference scheme of the proposed AdaBLDM algorithm. One can see that the whole procedure can be mainly divided into 4 stages, namely the pure denoising stage without editing; the latent editing stage; the image editing stage, and the decoder adaptation stage.

training, there is a 10% chance that an empty text prompt is input to the model. During the inference stage, we adopted the DDIM [39] sampling method with the normal denoising step $T_1 = 50$, the latent blended step $T_2 = 30$, and pixel blended step $T_3 = 5$. In the online decoder adaptation stage, $T_{ft} = 200$ and the conservative ratio $\lambda_{con} = 100$ to avoid overfitting to the anomaly-free region. The same optimizer as offline learning is used for this online adaptation except for the learning rate is set to 1×10^{-4} .

IV. EXPERIMENTS

A. Experiment Setting

1) *Evaluation Methodology*: In this section, we evaluate the proposed method for generating defective samples practically and extensively. In most AIGC applications, the appearance quality of the generated image, measured in either quantitative or qualitative ways, is the most important criterion to evaluate a generation algorithm. However, in the scenario of defective sample generation, we claim that a more important measuring standard is the improvement in AD accuracy. Consequently, a state-of-the-art anomaly detection algorithm, namely DeSTseg [6] is learned based on the augmented dataset, and the corresponding performance gain (if any) directly reflects the effectiveness of the synthetic samples. In addition, the classical Support Vector Machine (SVM) [55] is also employed as a complement to DeSTseg. Specifically, the SVM model is learned to classify the pixels into normal and anomalous, and in this way, a vanilla anomaly detection/localization method is obtained. The combination of the sophisticated (DeSTseg) and the naive (SVM) AD algorithms increases the comprehensiveness and thus the reliability of our experiment.

2) *Competitors*: We compare our defect generation algorithm with the cutting-edge generative models including DFM

[17] and DCDGANc [16] which is built based on StarGAN [56] or StyleGANv2 [34] algorithms. However, as the original StyleGANv2 in DCDGANc can easily lead to training crash according to our experiment, in this work, the StyleGANv2 is replaced by StyleGANv2-Ada [57] to ensure the stability of training. Furthermore, the results of the original DeSTseg algorithm, which also generates synthetic defects in the pasting fashion, are also compared. The training samples of the compared methods are strictly identical to those of AdaBLDM.

3) *Datasets*: To achieve a more general study, we perform the comparison on three well-known datasets, namely MVTEC-AD [22] (7 subcategories over 15), BTAD [58] (full dataset), and KSDD2 [59] which are introduced below.

- **MVTec AD** [22] is an open dataset containing ten object categories and five texture categories commonly seen, with up to eight defect categories for each object/texture category. All the images are accompanied by pixel-level masks showing the defect regions. Among the available defect categories, we opted to utilize defect categories that contain more than 10 defect images as the training dataset for our model. Specifically, we randomly selected 10 defect images per defect category from the test set and total defect-free images from the train set for model training and defect data generation. Due to time constraints, within the MVTEC AD dataset, we focused on evaluating our model using data from 2 Object categories (Hazelnut and Capsule) and 5 Texture categories.
- **BTAD** [58] comprises 2540 images from three categories of real-world industrial products with different body and surface defects. It is usually considered as a complementary dataset to the MVTEC AD when evaluating an AD algorithm. Consistent with MVTEC AD, we similarly opt for the selection of 10 instances of defect data along with defect-free data for the generation and training of the

model.

- **KSDD2** [59] with over 3000 images obtained while addressing a real-world industrial problem. This dataset comprises only one category, focusing on surface defects. For model training and data generation, we exclusively utilize the defect data and defect-free data from the training set.

To the best of our knowledge, the experiment of this paper involves much more subcategories, both in terms of number and variations, than any others in the current literature.

4) *Evaluation metrics for Anomaly Detection and Localization:*

- **Pixel-AUC** is the area under the receiver operating characteristic curve at the pixel level. It is the most popular AD measuring method while failing to reflect the real performance difference between algorithms when a serious class imbalance exists.
- **PRO** [60] on the contrary, focuses on the anomaly pixels and treats the AD performance on each anomaly region equally. Consequently, the PRO metric is more robust to the class imbalance which is a common situation in most AD benchmarks.
- **AP** [61] metric as a conventional metric for semantic segmentation, is frequently adopted in recently proposed AD algorithms. It reflects the anomaly detection performance from a pixel-level perspective.
- **IAP** [6] focus on instance recall as a more straightforward metric.
- **IAP90** For those applications requiring an extremely high recall, the precision at recall = k% is also computed and denoted as IAP@k, and k we follow [6] by setting k = 90 in our experiments.

5) *Evaluation metrics for generation quality:* Following the conventional evaluation manner for image generation algorithms, we here also compare the scores related to the quality of the generated images. In particular, the **Kernel Inception Distance (KID)** [62] as well as the **Learned Perceptual Image Patch Similarity (LPIPS)** [63] are involved in the comparison. In simple words, the former criterion reflects the generation's authenticity while the latter one indicates the generation's diversity.

6) *Training Settings for the Involved AD Models:* In our experiments, the generated samples are evaluated by using the simplest AD method and a sophisticated AD method. As one end of the spectrum, the SVM-based anomaly detection algorithm is extremely simple and thus can directly reflect the primitive quality of the generated images, at the patch level. In specific, the SVM model based on the RBF kernel [64] is employed as the patch classifier. The patch features are extracted by using the PatchCore algorithm [4] and each 768-D feature is assigned a positive label if the corresponding patch is normal while negative labels are assigned to the anomalous ones. In each trial, 100 images are randomly sampled from the synthetic defective images and then 5000 positive patch features and 5000 negative patch features are extracted for training the SVM model. The final performance on each subcategory is calculated by averaging the results of 10 random

trials with the same setting. Besides, the performance of the SVM model trained merely on the genuine defective data is also reported. As to the parameter setting, we by default set the γ of the RBF kernel as 1×10^{-4} while the regularization parameter C is set to 1.

Referring to DeSTseg [6] which employs a discriminative model to detect anomalous regions by comparing them with reconstructed defect-free counterparts, before training, we first generate 5000 defective samples by using AdaBLDM and another 5000 defective samples by using the data augmentation method of DeSTseg. We store the defective samples generated by AdaBLDM in \mathcal{D}_{gen} and store those augmented by DeSTseg in \mathcal{D}_{raw} . The training data is then sampled from the defect-free samples, \mathcal{D}_{raw} and \mathcal{D}_{gen} in the ratio of 5 : 4 : 1. Note that according to the methodology of DeSTseg, the genuine defective samples, which are the seeds of the synthetic data generation, can not be used for training as the anomaly-free version of them is unknown. For each subcategory, the DeSTseg is learned for 10000 iterations and we pick the DeSTseg model with a UNIQUE iteration number for all the subcategories in one dataset.

B. Quantitative Results

1) *Results on MVTec AD:* We first conduct the comparison of the SVM-based anomaly detection on the well-known MVTec AD dataset and report the results in Tab. IV-B1. From the table, we can see that the SVM achieves consistently best accuracies based on the samples generated by AdaBLDM. The genuine samples achieve the second-best performance while the samples obtained by comparing SOTA generation algorithms perform worse than the two aforementioned competitors.

On the other hand, Tab. IV-B1 illustrates the AD performances of DeSTseg based on the MVTec AD dataset. As shown in the table, the proposed method ranks the first for all the 5 AD metrics. In particular, the performance gains brought by the synthetic samples generated by AdaBLDM are 1.00%, 1.98% 6.68%, 6.35% and 7.93% on Pixel-AUC, PRO, AP, IAP, and IAP90, respectively. The significant improvements prove the validness of the proposed method.

2) *Results on BTAD and KSDD2:* Similarly, we compare the proposed method with other generation algorithms in terms of the AD performance on the other two well-known AD datasets. The accuracies obtained by DeSTseg are summarized in Tab. IV-B2 and Tab. IV-B2 for BTAD [58] and KSDD2 [59], respectively. One can again observe the remarkable superiority of the proposed method in the two tables. The artificial defects simulated by AdaBLDM lead to the best performances for all the involved AD metrics, on both two datasets.

3) *Image Quality:* Tab. IV-B3 demonstrates the scores on the image quality of the comparing generation algorithms. From the table, we can see that the proposed method achieves the best KID performances for most subcategories (except Grid and Wood) as well as the overall comparison. This is consistent with the AD performances reported in Tab. IV-B1 as the KID metric reflects the "reality" of the generated images.

In contrast, it is interesting to see that our method lead to poor LPIPS scores compared with other generation algorithms.

TABLE I

THE ANOMALY DETECTION AND LOCALIZATION PERFORMANCE OF SVM ON THE MVTEC AD DATASET, PIXEL-AUC/PRO/AP/IAP/IAP90, THE BEST AND THE SECOND-BEST NUMBERS ARE SHOWN IN RED AND BLUE, RESPECTIVELY.

Category	Genuine	DFM [17] (AAAI2023)	DCDGANc-StarGAN [16] (CVPRW2023)	DCDGANc-StyleGAN [16] (CVPRW2023)	AdaBLDM (ours)
Hazelnut	<u>98.07/70.03/47.07/94.85/63.03</u>	97.65/66.05/38.7/93.87/57.6	82.41/54.24/19.19/71.69/52.3	96.79/67.63/41.27/94.18/59.98	98.23/71.08/47.94/94.88/66.65
Wood	95.22/63.53/36.95/91.22/55.33	39.91/3.9/2.89/12.99/5.12	96.79/67.63/41.27/94.18/59.98	89.83/51.97/25.08/81.6/44.96	<u>95.96/71.02/48.83/93.05/63.41</u>
Capsule	92.28/13.91/6.65/84.01/12.31	91.72/37.37/9.01/87.36/25.69	99.51/71.09/52.11/99.14/61.98	94.05/37.13/10.47/89.09/28.15	<u>94.17/45.26/13.12/91.77/32.86</u>
Leather	99.07/62.88/40.86/98.52/51.21	45.15/3.05/0.66/29.62/2.25	89.83/51.97/25.08/81.6/44.96	99.51/71.09/52.11/99.14/61.98	<u>99.23/68.5/60.52/99.56/61.49</u>
Grid	89.02/28.68/2.87/75.29/23.78	73.75/3.53/0.78/47.6/3.7	93.66/ <u>46.29/19.09/83.09/45.71</u>	95.82/46.91/12.81/92.49/42.47	<u>95.22/35.31/7.55/89.01/32.86</u>
Tile	<u>93.94/74.81/49.55/87.72/68.71</u>	73.54/38.69/7.85/50.4/43.48	94.05/37.13/10.47/89.09/28.15	82.41/54.24/19.19/71.69/52.3	<u>92.74/71.86/47.4/85.9/68.46</u>
Carpet	95.22/ <u>63.53/36.95/91.22/55.33</u>	39.91/3.9/2.89/12.99/5.12	<u>95.54/44.8/13.12/91.49/40.75</u>	89.83/51.97/25.08/81.6/44.96	95.96/71.02/48.83/93.05/63.41
Average	<u>95.06/54.48/32.97/89.49/48.11</u>	72.09/24.93/9.76/54.7/22.52	93.11/53.31/25.76/87.18/47.69	93.23/54.0/26.34/87.62/48.1	95.95/57.69/35.51/91.57/52.53

TABLE II

THE ANOMALY DETECTION AND LOCALIZATION PERFORMANCE OF DeSTSEG ON THE MVTEC AD DATASET, PIXEL-AUC/PRO/AP/IAP/IAP90, THE BEST AND THE SECOND-BEST NUMBERS ARE SHOWN IN RED AND BLUE, RESPECTIVELY.

Category	DeSTSEG [6] (CVPR2023)	DFM [17] (AAAI2023)	DCDGANc-StarGAN [16] (CVPRW2023)	DCDGANc-StyleGAN [16] (CVPRW2023)	AdaBLDM (ours)
Hazelnut	99.65/97.46/88.22/89.06/75.58	99.45/98.01/88.5/90.48/ 82.32	99.53/97.69/87.47/87.78/74.17	99.62/98.1/90.31/90.69/80.78	99.65/98.65/91.27/91.47/81.96
Wood	95.72/93.0/73.62/79.77/63.6	97.91/97.09/83.78/ <u>92.49/85.63</u>	97.83/96.99/84.14/ 92.63/85.05	98.34/97.17/84.67/91.98/85.24	<u>98.23/97.23/84.59/90.85/82.47</u>
Capsule	99.21/96.29/57.79/52.7/33.32	98.43/95.39/ <u>62.89/58.5/31.82</u>	98.44/94.78/61.07/56.63/30.49	<u>98.85/95.77/62.08/57.28/34.16</u>	98.61/ <u>96.14/63.39/61.04/39.0</u>
Leather	99.76/99.06/75.0/74.96/64.92	99.81/99.42/80.08/83.28/72.91	99.84/99.56/82.53/86.47/76.82	99.84/99.5/81.7/83.64/74.32	99.84/99.56/82.62/85.89/73.51
Grid	<u>98.82/94.3/57.74/57.11/35.25</u>	98.24/ <u>94.38/56.0/57.38/26.34</u>	98.21/93.52/57.2/ <u>57.52/20.91</u>	97.88/91.47/56.4/55.95/13.72	98.95/96.21/60.65/62.87/31.11
Tile	98.7/97.28/93.12/96.38/ 92.33	98.68/96.77/92.87/95.58/88.65	99.04/97.54/ <u>94.1/96.41/90.38</u>	<u>99.1/97.69/93.97/96.27/90.24</u>	<u>99.17/97.86/94.57/96.61/90.14</u>
Carpet	94.86/92.99/69.74/84.79/58.4	97.89/96.64/78.99/88.6/74.26	98.18/97.08/81.45/89.28/76.53	<u>98.55/97.5/82.07/90.34/78.81</u>	99.33/98.47/84.87/90.53/80.77
Average	98.1/95.77/73.6/76.4/60.49	98.63/ <u>96.81/77.59/80.9/65.99</u>	98.72/96.73/78.28/ <u>90.96/64.91</u>	<u>98.88/96.74/78.74/80.88/65.32</u>	99.11/97.73/80.28/82.75/68.42

TABLE III

THE ANOMALY DETECTION AND LOCALIZATION PERFORMANCE OF DeSTSEG ON THE BTAD DATASET, PIXEL-AUC/PRO/AP/IAP/IAP90, THE BEST AND THE SECOND-BEST NUMBERS ARE SHOWN IN RED AND BLUE, RESPECTIVELY.

Category	DeSTSEG [6] (CVPR2023)	DFM [17] (AAAI2023)	DCDGANc-StarGAN [16] (CVPRW2023)	DCDGANc-StyleGAN [16] (CVPRW2023)	AdaBLDM (ours)
01	<u>96.25/82.5/45.74/39.93/26.95</u>	95.97/74.17/37.13/31.71/14.92	95.33/71.39/35.37/31.2/11.32	95.64/82.34/38.15/36.24/26.78	96.84/84.25/43.22/39.04/27.93
02	95.73/57.99/60.58/40.82/7.96	<u>96.15/64.78/62.73/47.46/12.61</u>	94.67/60.65/55.6/ 49.6/10.63	94.39/61.32/ <u>64.72/45.09/8.46</u>	96.55/65.46/70.16/47.99/13.24
03	99.47/98.01/44.29/35.87/17.54	98.94/95.45/39.13/34.18/ 19.22	98.92/95.32/37.26/35.82/ <u>18.02</u>	99.27/97.43/43.5/ <u>36.58/16.2</u>	99.47/97.97/45.91/36.59/17.95
Average	<u>97.15/79.5/50.2/38.87/17.48</u>	97.02/78.13/46.33/37.78/15.58	96.31/75.79/42.74/38.87/13.32	96.43/ <u>80.36/48.79/39.3/17.15</u>	97.62/82.56/53.1/41.21/19.71

TABLE IV

THE ANOMALY DETECTION AND LOCALIZATION PERFORMANCE OF DeSTSEG ON THE KSDD2 DATASET, PIXEL-AUC/PRO/AP/IAP/IAP90, THE BEST AND THE SECOND-BEST NUMBERS ARE SHOWN IN RED AND BLUE, RESPECTIVELY.

Method	Pixel AUC	PRO	AP	IAP	IAP90
DeSTSEG [6] (CVPR2023)	89.45	83.42	52.3	57.59	1.29
DFM [17] (AAAI2023)	86.69	85.53	47.38	54.39	1.26
DCDGANc-StarGAN [16] (CVPRW2023)	93.08	85.3	46.53	49.96	1.69
DCDGANc-StyleGAN [16] (CVPRW2023)	92.38	84.83	51.72	55.65	1.56
AdaBLDM (ours)	96.42	92.93	70.62	73.88	7.6

TABLE V

THE $KID \times 10^3 @ 5K \downarrow$ AND $LPIPS @ 5K \uparrow$ OF THE GENERATED IMAGES ON MVTEC AD, THE BEST AND THE SECOND-BEST NUMBERS ARE SHOWN IN RED AND BLUE, RESPECTIVELY

Category	DFM [17] (AAAI2023)	DCDGANc-StarGAN [16] (CVPRW2023)	DCDGANc-StyleGAN [16] (CVPRW2023)	AdaBLDM (ours)
Hazelnut	4.74/ 0.188	<u>1.76/0.16</u>	1.97/0.167	<u>1.72/0.182</u>
Wood	48.47/ 0.172	<u>7.91/0.046</u>	8.74/0.048	<u>2.74/0.076</u>
Capsule	3.66/0.018	<u>1.87/0.026</u>	1.08/0.026	4.14/ 0.027
Leather	61.35/ 0.199	<u>9.23/0.088</u>	13.6/0.078	5.85/0.032
Grid	<u>4.00/0.061</u>	2.04/0.073	7.21/ 0.087	5.38/0.07
Tile	<u>16.74/0.015</u>	23.16/0.036	21.5/ 0.05	<u>12.83/0.046</u>
Carpet	3.64/0.082	4.29/ 0.095	<u>3.61/0.088</u>	3.55/0.073
Average	20.37/ 0.105	<u>7.18/0.075</u>	8.25/ <u>0.078</u>	5.17/0.072

of AD models.

C. Qualitative Results

To offer readers a more direct impression of the proposed image generation algorithm, We hereby depict the generated defects by using the comparing methods in Fig. 4. One can see the proposed method, either with or without the online adaptation stage, can achieve significantly more lifelike images compared with other methods. In particular, only our method

Recall that either the editing process in the denoising stage or the online decoder adaptation prevents the generated image from being too diverse from the source image and the desired defect. *In this way, we claim that the poor image diversity might be a disadvantage of the proposed algorithm from the traditional perspective while it also implies a better-controlled generation process that can benefit the following training stage*

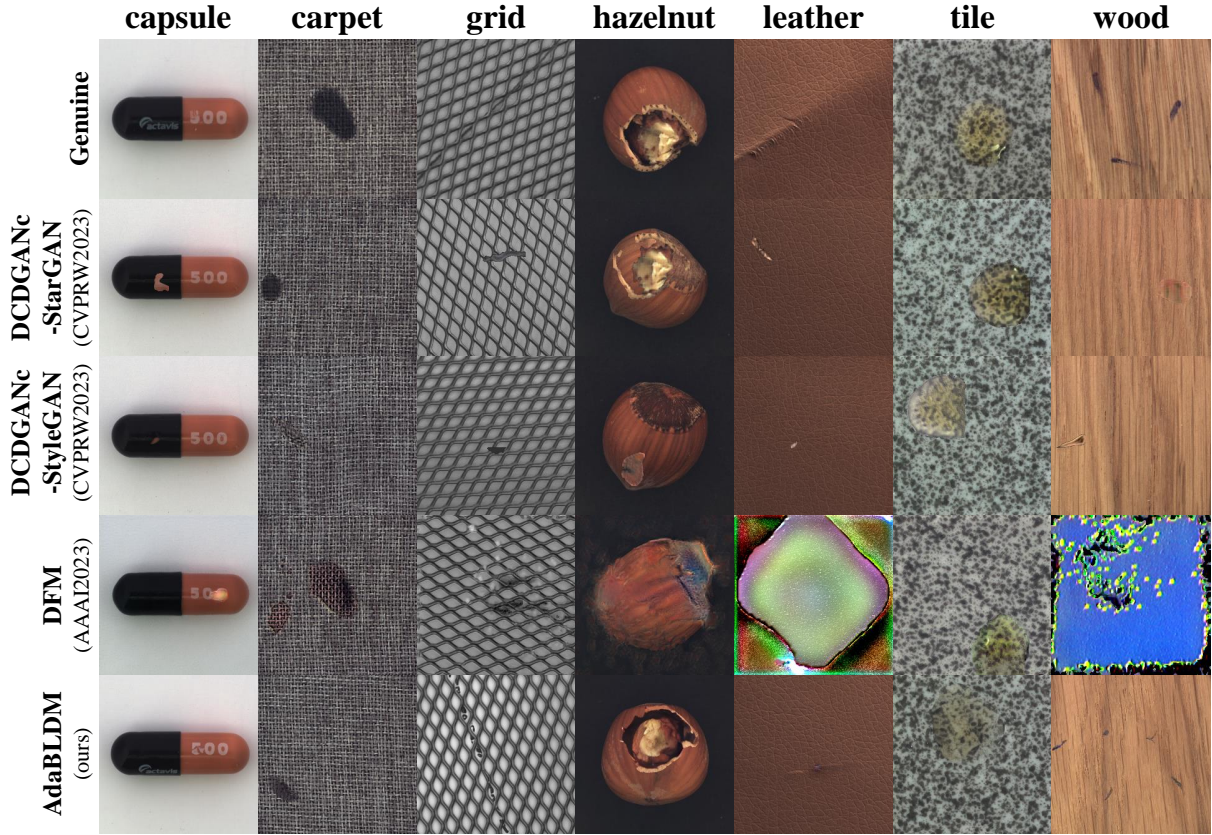


Fig. 4. The genuine and synthetic defective samples on MVtec AD dataset. From top to bottom, the samples with genuine defects; the samples generated by using DCDGANc-StarGAN; the samples generated by using DCDGANc-StyleGAN; the samples generated with DFM and the samples generated by using our method.

can generate the “crack” defects on the hazelnut subcategory. On the contrary, the DFM algorithm, though can generate synthetic defective samples with good quality in some scenarios, could fail in generation for some other cases.

We further compare with existing methods in fine-grained details, and experimental results are reported in Fig. 5. As shown in Fig. 5, the proposed method is more well-controlled in generating the defect regions with the specific category and location. In addition, the generated images with synthetic defects on BTAD and KSDD2 are shown in Fig. 6. It can be seen that besides MVtec AD, the image quality of AdaBLDM is maintained for the two different datasets.

Finally, as a qualitative complement to Tab. IV-B1, Fig. 7 shows the heat map of anomaly predicted by the DeSTseg algorithm. We can see that high-quality simulated synthetics benefits the AdaBLDM-equipped algorithm which can output competitive heat maps for anomaly detection and localization.

D. Ablation Study

In this section, we systematically evaluate the contribution of each component in our method. The following experiments are conducted:

- **Pretrain with domain knowledge**

As introduced in Sec. III-C, the denoising model $\epsilon_\theta(\cdot)$ is pretrained on the domain data. If this module is removed, AdaBLDM will rely on the prior knowledge from the

LAION-5B dataset [65], which might not highly correlate with the domain of industrial AD. Note that the pretraining is strictly independent to the current subcategory to maintain the fair comparison.

- **Image Editing**

Different from the conventional blended latent diffusion model, we propose to perform the intent editing in both latent space and pixel space (see Alg. 1). If this module is removed, the editing is only performed in the latent space.

- **Online Decoder Adaptation**

The online decoder adaptation is introduced in Alg. 2. The absence of this module results in a fixed image decoder.

The ablation results are summarized in Tab. VI. It is clear that as each module mentioned above is added to the algorithm, the corresponding AD performance increases steadily. In particular, the total performance improvements are 9.78% in AP, 14.46% in IAP, and 13.98% in IAP90, respectively.

V. CONCLUSION & FUTURE WORK

In this paper, we propose an advanced method to generate realistic defective samples for industrial anomaly detection and localization. Inspired by the diffusion model, we customize the Blended Latent Diffusion Model (BLDM) to be well-suited to this specific task. The proposed algorithm, termed

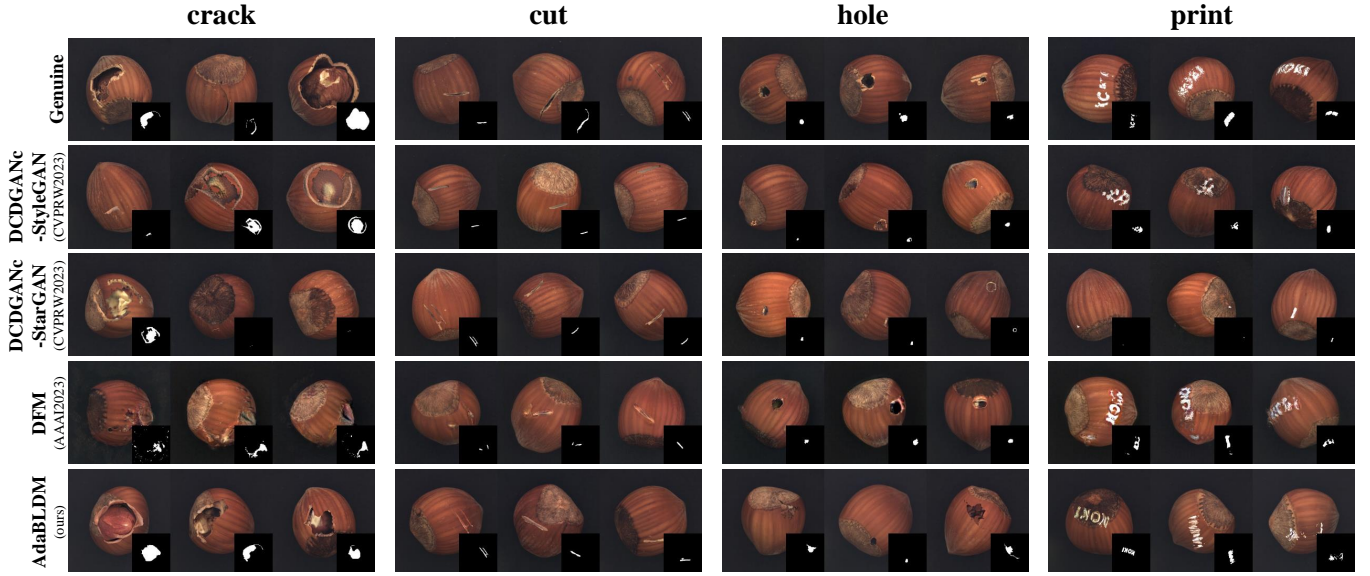


Fig. 5. The fine-grained comparison in the generation quality on the Hazelnut subcategory of MVtec AD. Different kinds of defects are mimicked by the involved generation algorithms and their performances can be compared on a more detailed level.

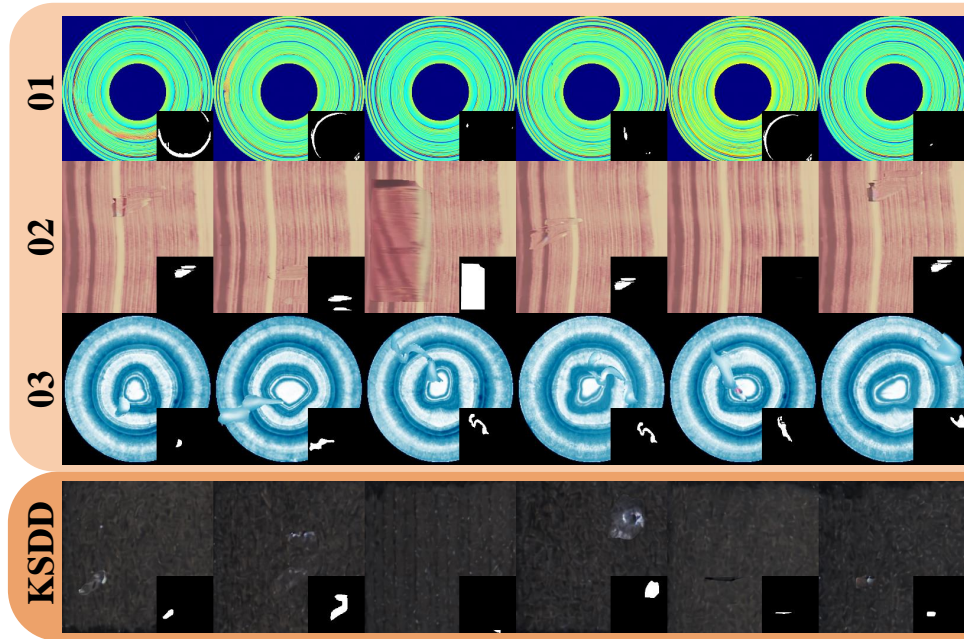


Fig. 6. The generation outputs of AdaBLDM on BTAD and KSDDV2 datasets.

TABLE VI
ABLATION STUDY OF ADABLDM

Modules			Performance				
Pretrain	Image Editing	Adaptation	Pixel auc	Pro	AP	IAP	IAP90
×	×	×	96.51	92.18	70.50	68.29	54.44
✓	×	×	97.23	93.14	71.21	69.30	58.32
✓	✓	×	99.12	97.49	80.25	82.36	67.65
✓	✓	✓	99.11	97.73	80.28	82.75	68.42

AdaBLDM, can generate better synthetic samples compared with existing methods based on conventional “cut-and-paste”

schemes or Generative Adversarial Networks (GANs). By applying the AdaBLDM in anomaly detection data augmenta-

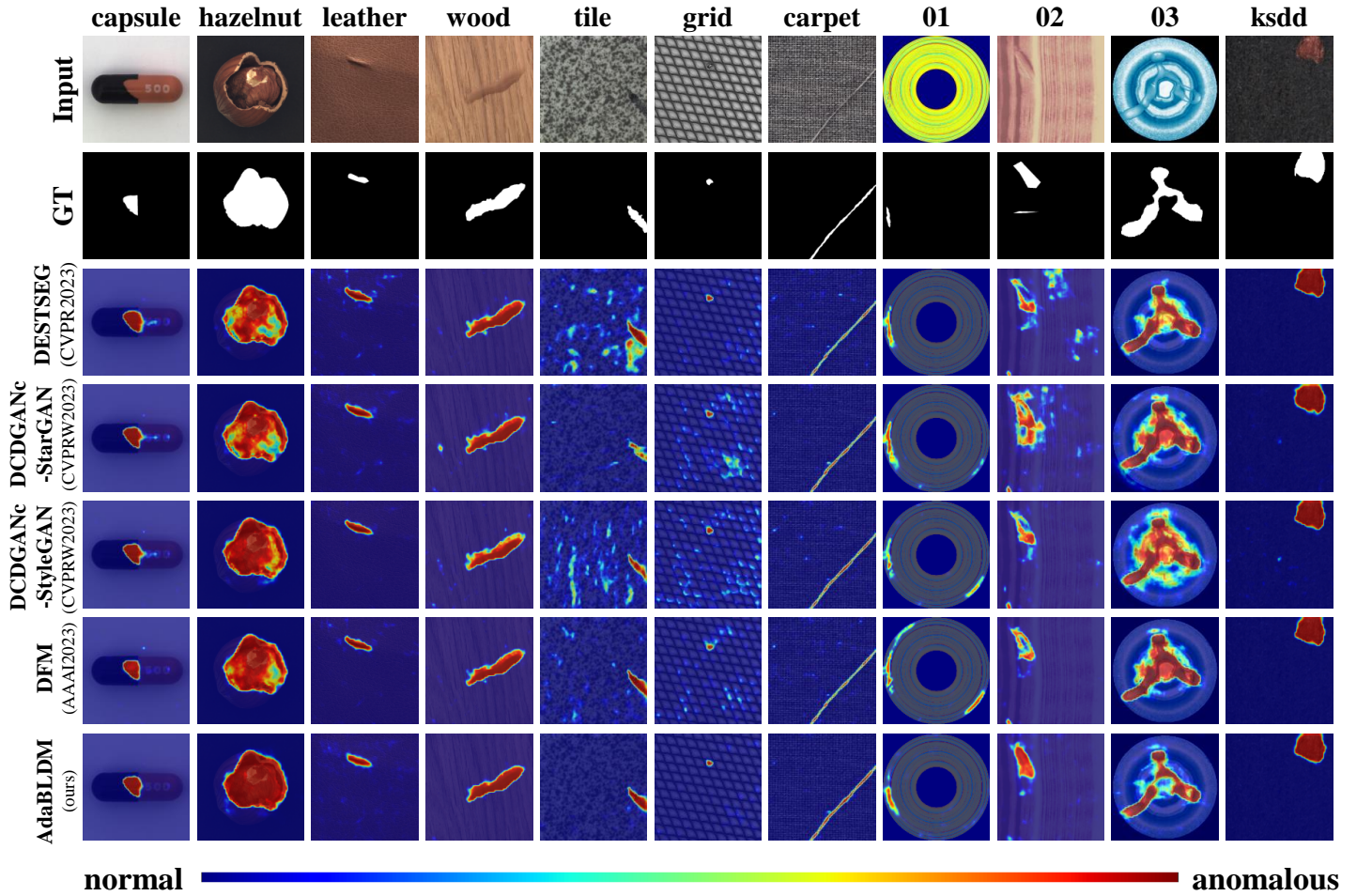


Fig. 7. Test results of different DeSTseg models learned based on the training sets obtained by using different generation methods. All the involved subcategories in this work (7 from MVTec AD, 3 from BTAD, and the only one in KSDDV2) are shown here.

tion, we achieve a state-of-the-art performance of AD, thanks to the well-controlled defective regions aligned at the pixel level. In the future, we explore high-quality synthetic defective samples by introducing finer controlling signals such as the language prompts describing the details (shape, size, etc.) of the demanding defects. Another appealing direction of future work is to speed up the denoising process of the diffusion model so that more defective samples can be generated given a limited time budget, which is a crucial constraint in most practical scenarios.

REFERENCES

- [1] H. M. Schlüter, J. Tan, B. Hou, and B. Kainz, “Natural synthetic anomalies for self-supervised anomaly detection and localization,” in *Proc. Eur. Conf. Comput. Vis.*, S. Avidan, G. Brostow, M. Cissé, G. M. Farinella, and T. Hassner, Eds. Cham: Springer Nature Switzerland, 2022, pp. 474–489. 1, 2
- [2] T. Defard, A. Setkov, A. Loesch, and R. Audigier, “Padim: a patch distribution modeling framework for anomaly detection and localization,” in *International Conference on Pattern Recognition*. Springer, 2021, pp. 475–489. 1, 2
- [3] V. Zavrtanik, M. Kristan, and D. Skočaj, “DrEm – a discriminatively trained reconstruction embedding for surface anomaly detection,” in *Proc. IEEE Int. Conf. Comput. Vis.*, 2021, pp. 8310–8319. 1, 2
- [4] K. Roth, L. Pemula, J. Zepeda, B. Schölkopf, T. Brox, and P. Gehler, “Towards total recall in industrial anomaly detection,” in *Proc. IEEE Conf. Comput. Vis. Pattern Recog.*, June 2022, pp. 14 318–14 328. 1, 7
- [5] M. Yang, P. Wu, and H. Feng, “Memseg: A semi-supervised method for image surface defect detection using differences and commonalities,” *Eng. Appl. Artif.*, vol. 119, p. 105835, 2023. 1, 2
- [6] X. Zhang, S. Li, X. Li, P. Huang, J. Shan, and T. Chen, “Destseg: Segmentation guided denoising student-teacher for anomaly detection,” in *Proc. IEEE Conf. Comput. Vis. Pattern Recog.*, 2023, pp. 3914–3923. 1, 2, 5, 6, 7, 8
- [7] W. Liu, H. Chang, B. Ma, S. Shan, and X. Chen, “Diversity-measurable anomaly detection,” in *Proc. IEEE Conf. Comput. Vis. Pattern Recog.*, 2023, pp. 12 147–12 156. 1
- [8] Q. Zhou, S. He, H. Liu, T. Chen, and J. Chen, “Pull & push: Leveraging differential knowledge distillation for efficient unsupervised anomaly detection and localization,” *IEEE Trans. Circuit Syst. Video Technol.*, vol. 33, no. 5, pp. 2176–2189, 2023. 1
- [9] K. Wu, L. Zhu, W. Shi, W. Wang, and J. Wu, “Self-attention memory-augmented wavelet-cnn for anomaly detection,” *IEEE Trans. Circuit Syst. Video Technol.*, vol. 33, no. 3, pp. 1374–1385, 2023. 1
- [10] H. Yao, W. Yu, W. Luo, Z. Qiang, D. Luo, and X. Zhang, “Learning global-local correspondence with semantic bottleneck for logical anomaly detection,” *IEEE Trans. Circuit Syst. Video Technol.*, pp. 1–1, 2023. 1
- [11] B. Scholkopf, R. Williamson, A. Smola, J. Shawe-Taylor, J. Platt *et al.*, “Support vector method for novelty detection,” *Proc. Adv. Neural Inf. Process. Syst.*, vol. 12, no. 3, pp. 582–588, 2000. 1
- [12] V. Chandola, A. Banerjee, and V. Kumar, “Anomaly detection: A survey,” *ACM computing surveys (CSUR)*, vol. 41, no. 3, pp. 1–58, 2009. 1
- [13] C. Huang, Z. Kang, and H. Wu, “A prototype-based neural network for image anomaly detection and localization,” *arXiv:2310.02576*, 2023. 1
- [14] H. Li, J. Hu, B. Li, H. Chen, Y. Zheng, and C. Shen, “Target before shooting: Accurate anomaly detection and localization under one mil-

- lisecond via cascade patch retrieval,” *arXiv:2308.06748*, 2023. 1, 4, 5
- [15] H. Li, J. Wu, H. Chen, M. Wang, and C. Shen, “Efficient anomaly detection with budget annotation using semi-supervised residual transformer,” *arXiv:2306.03492*, 2023. 1
- [16] J. Wei, F. Shen, C. Lv, Z. Zhang, F. Zhang, and H. Yang, “Diversified and multi-class controllable industrial defect synthesis for data augmentation and transfer,” in *IEEE Conf. Comput. Vis. Pattern Recog. Worksh.*, 2023, pp. 4444–4452. 2, 6, 8
- [17] Y. Duan, Y. Hong, L. Niu, and L. Zhang, “Few-shot defect image generation via defect-aware feature manipulation,” in *AAAI Conf. Artif. Intell.*, vol. 37, no. 1, 2023, pp. 571–578. 2, 6, 8
- [18] J. Sohl-Dickstein, E. Weiss, N. Maheswaranathan, and S. Ganguli, “Deep unsupervised learning using nonequilibrium thermodynamics,” in *Int. Conf. Mach. Learn.*. PMLR, 2015, pp. 2256–2265. 2, 3
- [19] R. Rombach, A. Blattmann, D. Lorenz, P. Esser, and B. Ommer, “High-resolution image synthesis with latent diffusion models,” in *Proc. IEEE Conf. Comput. Vis. Pattern Recog.*, 2022, pp. 10684–10695. 2, 3, 4, 5
- [20] O. Avrahami, D. Lischinski, and O. Fried, “Blended diffusion for text-driven editing of natural images,” in *Proc. IEEE Conf. Comput. Vis. Pattern Recog.*, 2022, pp. 18208–18218. 2, 3, 5
- [21] O. Avrahami, O. Fried, and D. Lischinski, “Blended latent diffusion,” *ACM Trans. Graph.*, vol. 42, no. 4, pp. 1–11, 2023. 2, 3, 4
- [22] P. Bergmann, M. Fauser, D. Sattlegger, and C. Steger, “Mvtec ad—a comprehensive real-world dataset for unsupervised anomaly detection,” in *Proc. IEEE Conf. Comput. Vis. Pattern Recog.*, 2019, pp. 9592–9600. 2, 4, 6
- [23] F. Xue, Y. Li, D. L. Y. Xie, L. Wu, and R. Hong, “Lipformer: Learning to lipread unseen speakers based on visual-landmark transformers,” *IEEE Trans. Circuit Syst. Video Technol.*, vol. 33, no. 9, pp. 4507–4517, 2023. 2
- [24] T. DeVries and G. W. Taylor, “Improved regularization of convolutional neural networks with dropout,” *arXiv:1708.04552*, 2017. 2
- [25] C.-L. Li, K. Sohn, J. Yoon, and T. Pfister, “Cutpaste: Self-supervised learning for anomaly detection and localization,” in *Proc. IEEE Conf. Comput. Vis. Pattern Recog.*, 2021, pp. 9664–9674. 2
- [26] D. Lin, Y. Cao, W. Zhu, and Y. Li, “Few-shot defect segmentation leveraging abundant defect-free training samples through normal background regularization and crop-and-paste operation,” in *Proc. IEEE Int. Conf. Multimedia Expo.*, 2021, pp. 1–6. 2
- [27] H. Zhang, Z. Wu, Z. Wang, Z. Chen, and Y.-G. Jiang, “Prototypical residual networks for anomaly detection and localization,” in *Proc. IEEE Conf. Comput. Vis. Pattern Recog.*, 2023, pp. 16281–16291. 2
- [28] J. Niu, Q. Yu, S. Dong, Z. Wang, K. Dang, and xiaowei ding, “Resynthdetect: A fundus anomaly detection network with reconstruction and synthetic features,” in *Brit. Mach. Vis. Conf.*. BMVA, 2023. 2
- [29] W. Xia, Y. Zhang, Y. Yang, J.-H. Xue, B. Zhou, and M.-H. Yang, “Gan inversion: A survey,” *IEEE Trans. Pattern Anal. Mach. Intell.*, vol. 45, no. 3, pp. 3121–3138, 2022. 2
- [30] S. Niu, B. Li, X. Wang, and H. Lin, “Defect image sample generation with gan for improving defect recognition,” *IEEE Transactions on Automation Science and Engineering*, vol. 17, no. 3, pp. 1611–1622, 2020. 2
- [31] L. Wu, R. Hong, Y. Wang, and M. Wang, “Cross-entropy adversarial view adaptation for person re-identification,” *IEEE Trans. Circuit Syst. Video Technol.*, vol. 30, no. 7, pp. 2081–2090, 2020. 2
- [32] L. Yang, Z. Zhang, Y. Song, S. Hong, R. Xu, Y. Zhao, W. Zhang, B. Cui, and M.-H. Yang, “Diffusion models: A comprehensive survey of methods and applications,” *ACM Computing Surveys*, vol. 56, no. 4, pp. 1–39, 2023. 2
- [33] G. Zhang, K. Cui, T.-Y. Hung, and S. Lu, “Defect-gan: High-fidelity defect synthesis for automated defect inspection,” in *IEEE/CVF Winter Conference on Applications of Computer Vision*, 2021, pp. 2523–2533. 2
- [34] T. Karras, S. Laine, M. Aittala, J. Hellsten, J. Lehtinen, and T. Aila, “Analyzing and improving the image quality of stylegan,” *Proc. IEEE Conf. Comput. Vis. Pattern Recog.*, pp. 8107–8116, 2019. 2, 6
- [35] I. Goodfellow, J. Pouget-Abadie, M. Mirza, B. Xu, D. Warde-Farley, S. Ozair, A. Courville, and Y. Bengio, “Generative adversarial nets,” *Proc. Adv. Neural Inf. Process. Syst.*, vol. 27, 2014. 3
- [36] D. P. Kingma and M. Welling, “Auto-encoding variational bayes,” *arXiv:1312.6114*, 2013. 3
- [37] L. Dinh, D. Krueger, and Y. Bengio, “Nice: Non-linear independent components estimation,” *arXiv:1410.8516*, 2014. 3
- [38] J. Ho, A. Jain, and P. Abbeel, “Denoising diffusion probabilistic models,” *Proc. Adv. Neural Inf. Process. Syst.*, vol. 33, pp. 6840–6851, 2020. 3, 5
- [39] J. Song, C. Meng, and S. Ermon, “Denoising diffusion implicit models,” *arXiv:2010.02502*, 2020. 3, 5, 6
- [40] P. Dhariwal and A. Nichol, “Diffusion models beat gans on image synthesis,” *Proc. Adv. Neural Inf. Process. Syst.*, vol. 34, pp. 8780–8794, 2021. 3
- [41] A. Ramesh, P. Dhariwal, A. Nichol, C. Chu, and M. Chen, “Hierarchical text-conditional image generation with clip latents,” *arXiv:2204.06125*, vol. 1, no. 2, p. 3, 2022. 3
- [42] C. Saharia, W. Chan, S. Saxena, L. Li, J. Whang, E. L. Denton, K. Ghasemipour, R. Gontijo Lopes, B. Karagol Ayan, T. Salimans *et al.*, “Photorealistic text-to-image diffusion models with deep language understanding,” *Proc. Adv. Neural Inf. Process. Syst.*, vol. 35, pp. 36479–36494, 2022. 3
- [43] A. Lugmayr, M. Danelljan, A. Romero, F. Yu, R. Timofte, and L. Van Gool, “Repaint: Inpainting using denoising diffusion probabilistic models,” in *Proc. IEEE Conf. Comput. Vis. Pattern Recog.*, 2022, pp. 11461–11471. 3
- [44] M. Kim, F. Liu, A. Jain, and X. Liu, “Dcfac: Synthetic face generation with dual condition diffusion model,” in *Proc. IEEE Conf. Comput. Vis. Pattern Recog.*, 2023, pp. 12715–12725. 3
- [45] L. Zhang, A. Rao, and M. Agrawala, “Adding conditional control to text-to-image diffusion models,” *Proc. IEEE Int. Conf. Comput. Vis.*, pp. 3813–3824, 2023. 3
- [46] Z. Yang, T. Chu, X. Lin, E. Gao, D. Liu, J. Yang, and C. Wang, “Eliminating contextual prior bias for semantic image editing via dual-cycle diffusion,” *IEEE Trans. Circuit Syst. Video Technol.*, vol. 34, no. 2, pp. 1316–1320, 2024. 3
- [47] W. Wu, Y. Zhao, H. Chen, Y. Gu, R. Zhao, Y. He, H. Zhou, M. Z. Shou, and C. Shen, “Datasetdm: Synthesizing data with perception annotations using diffusion models,” *Proc. Adv. Neural Inf. Process. Syst.*, vol. 36, 2024. 3
- [48] J. Wyatt, A. Leach, S. M. Schmon, and C. G. Willcocks, “Anoddp: Anomaly detection with denoising diffusion probabilistic models using simplex noise,” in *Proc. IEEE Conf. Comput. Vis. Pattern Recog.*, 2022, pp. 650–656. 3
- [49] X. Zhang, N. Li, J. Li, T. Dai, Y. Jiang, and S.-T. Xia, “Unsupervised surface anomaly detection with diffusion probabilistic model,” in *Proc. IEEE Int. Conf. Comput. Vis.*, 2023, pp. 6782–6791. 3
- [50] J. Wolleb, F. Bieder, R. Sandkühler, and P. C. Cattin, “Diffusion models for medical anomaly detection,” in *International Conference on Medical image computing and computer-assisted intervention*. Springer, 2022, pp. 35–45. 3
- [51] H. Xu, S. Xu, and W. Yang, “Unsupervised industrial anomaly detection with diffusion models,” *Journal of Visual Communication and Image Representation*, vol. 97, p. 103983, 2023. 3
- [52] A. Radford, J. W. Kim, C. Hallacy, A. Ramesh, G. Goh, S. Agarwal, G. Sastry, A. Askell, P. Mishkin, J. Clark, G. Krueger, and I. Sutskever, “Learning transferable visual models from natural language supervision,” in *Int. Conf. Mach. Learn.*, 2021. 4
- [53] A. Van Den Oord, O. Vinyals *et al.*, “Neural discrete representation learning,” *Proc. Adv. Neural Inf. Process. Syst.*, vol. 30, 2017. 4
- [54] I. Loshchilov and F. Hutter, “Decoupled weight decay regularization,” in *Proc. Int. Conf. Learn. Represent.*, 2017. 5
- [55] C. Cortes and V. Vapnik, “Support-vector networks,” *Machine learning*, vol. 20, pp. 273–297, 1995. 6
- [56] Y. Choi, Y. Uh, J. Yoo, and J.-W. Ha, “Stargan v2: Diverse image synthesis for multiple domains,” in *Proc. IEEE Conf. Comput. Vis. Pattern Recog.*, 2020, pp. 8188–8197. 6
- [57] T. Karras, M. Aittala, J. Hellsten, S. Laine, J. Lehtinen, and T. Aila, “Training generative adversarial networks with limited data,” in *Proc. Adv. Neural Inf. Process. Syst.*, H. Larochelle, M. Ranzato, R. Hadsell, M. Balcan, and H. Lin, Eds., vol. 33. Curran Associates, Inc., 2020, pp. 12104–12114. 6
- [58] P. Mishra, R. Verk, D. Fornasier, C. Piciarelli, and G. L. Foresti, “Vt-adl: A vision transformer network for image anomaly detection and localization,” in *International Symposium on Industrial Electronics*. IEEE, 2021, pp. 01–06. 6, 7
- [59] J. Božić, D. Tabernik, and D. Škočaj, “Mixed supervision for surface-defect detection: From weakly to fully supervised learning,” *Computers in Industry*, vol. 129, p. 103459, 2021. 6, 7
- [60] P. Bergmann, M. Fauser, D. Sattlegger, and C. Steger, “Uninformed students: Student-teacher anomaly detection with discriminative latent embeddings,” in *Proc. IEEE Conf. Comput. Vis. Pattern Recog.*, 2020, pp. 4183–4192. 7
- [61] T. Saito and M. Rehmsmeier, “The precision-recall plot is more informative than the roc plot when evaluating binary classifiers on imbalanced datasets,” *PloS one*, vol. 10, no. 3, p. e0118432, 2015. 7

- [62] M. Bińkowski, D. J. Sutherland, M. Arbel, and A. Gretton, “Demystifying mmd gans,” 2018. 7
- [63] R. Zhang, P. Isola, A. A. Efros, E. Shechtman, and O. Wang, “The unreasonable effectiveness of deep features as a perceptual metric,” in *Proc. IEEE Conf. Comput. Vis. Pattern Recog.*, 2018, pp. 586–595. 7
- [64] K.-M. Chung, W.-C. Kao, C.-L. Sun, L.-L. Wang, and C.-J. Lin, “Radius margin bounds for support vector machines with the rbf kernel,” *Neural computation*, vol. 15, no. 11, pp. 2643–2681, 2003. 7
- [65] C. Schuhmann, R. Beaumont, R. Vencu, C. Gordon, R. Wightman, M. Cherti, T. Coombes, A. Katta, C. Mullis, M. Wortsman *et al.*, “Laion-5b: An open large-scale dataset for training next generation image-text models,” *Proc. Adv. Neural Inf. Process. Syst.*, vol. 35, pp. 25 278–25 294, 2022. 9